

Generation of a Hybrid DSMC/CFD Solution for Gas Mixtures with Internal Degrees of Freedom

Kelly A. Stephani*, David B. Goldstein[†] and Philip L. Varghese[‡]

Department of Aerospace Engineering, The University of Texas at Austin, Austin, TX, 78712, USA

A consistent approach for generating a hybrid DSMC/CFD solution is presented for re-entry applications involving neutral gas mixtures with internal energy. A quality hybrid solution requires consistency in the thermo-chemical models employed by the particle (DSMC) and continuum (CFD) solvers, as well as an appropriate boundary condition for the transfer of flux information across the hybrid interface. The first half of this work focuses on achieving consistency in the transport properties obtained by particle and continuum solvers, including species diffusion, viscosity and translational and internal thermal conductivities for a five-species air mixture. In the second portion, a new approach for the generation of particles at a hybrid interface is presented for gas mixtures with internal degrees of freedom. Particle thermal velocities and internal energies are prescribed from the appropriate non-equilibrium (perturbed) distribution, in which diffusion, shear stress and heat flux terms are included in the Generalized Chapman-Enskog formulation of the perturbation. The significance of the contributions from these terms on the perturbation are examined at a hybrid interface within non-equilibrium boundary layer flow, as well as within the breakdown region near a normal shock, in a five-species air gas mixture. The validity of the Chapman-Enskog perturbation at each of these hybrid interfaces is assessed by comparison with the Generalized Chapman-Enskog perturbations.

Nomenclature

α	VSS exponent
\mathbb{D}_i	scaled diffusion flux
$\tau_{ij,s}$	scaled shear stress
$q_{i,s}$	scaled translational heat flux
$\tilde{q}_{i,s}$	scaled internal heat flux
d_{ref}	reference diameter
T_{ref}	reference temperature
ω	temperature exponent
α	VSS scattering exponent
g	relative molecular collision speed
D_s	effective diffusion coefficient
\mathcal{D}_{st}	binary diffusion coefficient
χ	mole fraction
Y	mass fraction

*Ph.D. Candidate, Department of Aerospace Engineering, 210 E. 24th St. Austin, TX, Student Member AIAA.

[†]Professor, Department of Aerospace Engineering, 210 E. 24th St. Austin, TX, Senior Member AIAA.

[‡]Professor and Department Chair, Department of Aerospace Engineering, 210 E. 24th St. Austin, TX, Associate Fellow AIAA.

w	weighting factor
ρ	density
M	molar mass
k_b	Boltzmann constant
n	number density
T	temperature
m^*	reduced mass
$\Omega^l(r)$	collision integral (l, r from Sonine polynomial expansion)
m	molecular mass
A, B	ratio of collision integrals
μ	viscosity coefficient
K	conductivity coefficient
c_v	specific heat (constant volume, or internal)
p	pressure
g_{int}	degeneracy of internal level
Z	partition function
$f^{(0)}$	equilibrium Maxwell-Boltzmann distribution function
$f^{(1)}$	non-equilibrium distribution function
\mathbf{C}	thermal velocity vector, $\mathbf{C} = (C_x, C_y, C_z)$
\mathcal{C}	scaled thermal velocity
β	inverse most probable thermal speed
\mathcal{E}	scaled internal energy
ϵ_{int}	internal energy
ϕ	perturbation
Γ	perturbation function
u, v, w	bulk velocity components
Θ_v	characteristic vibrational temperature
<i>Subscript</i>	
s, t	species indices, $s, t \in \mathbb{S}$
i, j	cartesian coordinate index, $i, j \in (x, y, z)$
int	internal mode (rot=rotational, vib=vibrational)
w	wall condition
CE	Chapman-Enskog
GCE	Generalized Chapman-Enskog

I. Introduction

Flows generated around vehicles during hypersonic re-entry or high-altitude flight are often characterized by multi-scale, multi-physics phenomena, and may include regions of both near-continuum and non-equilibrium flow. While the details of non-equilibrium processes are established at the microscopic scale,

their influence on the macroscopic description of the overall system, including heat loads, aerodynamics, and gas/surface interactions, can be substantial. Thus, the ability to accurately model these multi-scale flows is necessary to inform important design decisions.

Although CFD approaches provide an efficient and accurate solution in near-continuum flow regimes, the underlying continuum assumption inherent in the solution of the Navier-Stokes equations breaks down in non-equilibrium flows. In this regime, high-fidelity kinetics-based methods, such as direct simulation Monte Carlo (DSMC),¹ must be used to accurately capture non-equilibrium effects that drive important thermo-chemical processes. While the DSMC solution is valid from free-molecular to continuum regimes, the time step and cell size requirements become computationally prohibitive in the continuum limit. It is precisely in this regime, however, that a CFD solver may be employed. Thus, a combined DSMC/CFD hybrid approach is often adopted as a way to achieve high-fidelity solutions while maintaining computational efficiency.

Hybrid methods have been developed and successfully applied for a variety of flow scenarios.²⁻⁹ The hybrid flowfield solution is generally obtained by first determining the location of the hybrid interface, which forms the boundary between the CFD and DSMC solvers, at or near the breakdown of the Navier-Stokes solution. Since the breakdown location can not be determined *a priori*, an initial CFD solution is generally used to determine the interface location based on a breakdown criterion. This criterion may be either parameter-based, or based on a direct comparison of flow quantities or distributions.^{5,10-13} The interface is then used to pass flowfield information between the two solvers. Macroscopic flowfield quantities from the CFD solution are used to prescribe the appropriate distribution function from which DSMC particle thermal velocities and internal energies are sampled. These particles may be created and fluxed into the non-equilibrium computational domain using either volume reservoir or surface reservoir approaches. The DSMC solver is then used to generate the local non-equilibrium flow solution.

The generation of hybrid solutions that involve the coupling of DSMC and CFD solutions requires a careful and consistent formulation of a proper boundary condition for the transfer of flux information across the hybrid interface. In equilibrium conditions (i.e., $\mathbb{D}_i = \tau_{ij} = q_i = 0$, or Euler solution), DSMC particle information may be sampled from an equilibrium Maxwell-Boltzmann distribution. Under non-equilibrium conditions, however, (i.e., $\mathbb{D}_i, \tau_{ij}, q_i \neq 0$, or Navier-Stokes solution) DSMC particle information must be sampled from the Chapman-Enskog distribution, to ensure the preservation of flux information across the hybrid interface. Garcia and Alder presented an acceptance-rejection algorithm for generating particle velocities from a Chapman-Enskog distribution within a volume reservoir.¹⁴ This formulation, however, is limited to simple (single-species, monatomic) gas flows, and includes only the shear stress tensor and translational heat flux vector components in the expression for the perturbation. In efforts to extend these hybrid methods to more complex flows often encountered in hypersonic applications, this work presents an extension of the Chapman-Enskog boundary condition to include gas mixtures and gases with internal energy. This new boundary condition is formulated in the framework of Generalized Chapman-Enskog Theory,¹⁵⁻¹⁷ and includes contributions from Navier-Stokes fluxes arising from species diffusion, viscosity, and translational and internal thermal conductivity.

An additional consideration that is necessary for a quality hybrid solution is the consistent treatment of the thermo-chemical models employed by each of the solvers. For simulations of hypersonic flows, this includes models for thermal relaxation and general thermodynamics, chemical reactions, and mass, momentum and energy transport. Consistency in these models promotes a smooth transition from one computational region to the other by ensuring that the same flow ‘problem’ is being solved in each region. It also allows for a consistent comparison of the CFD and DSMC solutions by ensuring that any differences between the solutions are due to fundamental non-equilibrium processes, rather than differences in the physical models. Previous studies have presented consistent treatments for the thermal relaxation processes^{18,19} and chemical reactions in five-species air systems²⁰ for use in hybrid applications, or direct DSMC/CFD comparisons. This manuscript examines the transport properties generated by the DSMC and CFD models for a five-species air gas mixture. A general approach for the calibration of the DSMC collision model parameters is presented, in which both the variable hard sphere (VHS) and variable soft sphere (VSS) collision cross section models are examined. The method for prescribing the collision partner parameters (either collision-averaged or collision-specific) is also examined in the fitting of DSMC transport coefficients. The resulting transport coefficients from the calibrated DSMC parameters are compared with the transport coefficient models employed in the CFD solver.

II. Consistent Treatment of Transport Properties

The aim of this section is to establish a general approach for achieving consistency in the transport properties between DSMC and CFD solvers. To this end, it is assumed that the transport coefficients determined from the CFD transport models serve as the ‘standard’ values of diffusion, viscosity and thermal conductivity. The transport coefficients from DSMC are computed from Chapman-Enskog theory in which the collision integrals are expressed in terms of the VHS and VSS collision cross section models.

Various models are available for computing the mass diffusion, viscosity and thermal conductivity coefficients in continuum CFD solvers. In this work, the diffusion coefficients are determined using the self-consistent effective binary diffusion (SCEBD) model, and the viscosity and thermal conductivity coefficients are determined by the Gupta-Yos approximate mixing rules.^{21,22} The transport properties within the Gupta-Yos model are determined from expressions involving the collision integrals, $\Omega_{st}^1(1)$ and $\Omega_{st}^2(2)$, and a curve-fit is employed to obtain these collision integrals as a function of temperature.

The transport properties in DSMC are a result of the transfer of mass, momentum and energy through particle movement and collision dynamics as determined by the collision model. DSMC uses a variety of collision models, including variable hard sphere (VHS) and variable soft sphere (VSS) models, in which the simulation particles are modeled as hard spheres of diameter d which is a function of g , the relative speed of the collision pair, such that $d \sim (1/g)^{\omega-1/2}$. The VSS model also includes a scattering angle specified by the coefficient α , such that values of $\alpha > 1.0$ result in a scattering angle smaller than the corresponding value of the VHS model (in which $\alpha = 1.0$). The reduced scattering angle effectively establishes a forward-scattering tendency of the colliding particles. This feature in VSS provides a model in which both the diffusion and viscosity cross sections are consistent with those from the inverse power law potential.²³

The fitting of the DSMC transport coefficients to the CFD values is achieved through application of the Nelder-Mead Simplex Method,^{24,25} which is used to determine the set of VHS and VSS model parameters that provide the best fit in the transport coefficients.²⁶ Before doing this, we first present the expressions used to determine the DSMC mixture diffusion, viscosity and thermal conductivity coefficients based on the VHS and VSS models.

To allow for a consistent comparison to the SCEBD species diffusion model used in the CFD solver, we compute the effective diffusivities D_s from DSMC according to:²²

$$D_s = \left(1 - \frac{w_s}{w}\right) \left(\sum_{t \neq s} \frac{\chi_t}{\mathcal{D}_{st}}\right)^{-1}. \quad (1)$$

Here, χ_t is the mole fraction of species t , w and w_s represent the weighting factors defined as:

$$w_s = \frac{\rho_s}{\sqrt{M_s}}, \quad (2)$$

$$w = \sum_s w_s. \quad (3)$$

In (2), ρ_s is the density of species s , M_s is the molar mass of species s , and \mathcal{D}_{st} is the binary diffusion coefficient for species pair s, t :

$$\mathcal{D}_{st} = \frac{3k_b T}{16nm_{st}^* \Omega_{st}^1(1)}. \quad (4)$$

In (4), k_b is Boltzmann’s constant, n and T are the number density and temperature, respectively, and m_{st}^* is the reduced mass. In the case of the species diffusion, it would be best to use the full matrix of multicomponent diffusion coefficients, D_{st} , in the fitting process directly, rather than using the effective binary diffusion coefficients as shown in (1). However, the Navier-Stokes solver considered in this work employs the SCEBD model in determining the diffusion mass flux, which uses a mixing rule to approximate the full multicomponent diffusion coefficient matrix as five effective binary diffusion coefficients, D_s . We therefore adopt this model to represent the species diffusion coefficients from DSMC, allowing for a consistent comparison between the two solvers.

The DSMC mixture viscosity can be determined from the first-order approximation of the mixture viscosity which is defined as:²⁷

$$[\mu]_1 = \sum_s b_s. \quad (5)$$

The quantity b_s is the contribution of each species to the overall mixture viscosity and may be determined by solving the following system:²⁷

$$\chi_s = b_s \left\{ \frac{\chi_s}{[\mu_s]_1} + \sum_{t \neq s} \frac{3\chi_t}{(\rho'_s + \rho'_t)\mathcal{D}_{st}} \left(\frac{2}{3} + \frac{m_t}{m_s} A_{st} \right) \right. \\ \left. - \chi_s \sum_{t \neq s} \frac{3b_t}{(\rho'_s + \rho'_t)\mathcal{D}_{st}} \left(\frac{2}{3} - A_{st} \right) \right\}. \quad (6)$$

The quantities μ_s and A_{st} in (6) represent the viscosity of species s when pure and the first ratio of collision integrals, respectively, and are defined as:

$$[\mu_s]_1 = \frac{5k_b T}{8\Omega_1^2(2)}, \quad (7)$$

$$A_{st} = \frac{\Omega_{st}^2(2)}{5\Omega_{st}^1(1)}. \quad (8)$$

The terms ρ'_s, ρ'_t refer to the density of species (s, t) when pure at the pressure and temperature of the actual gas mixture, and m_s, m_t are the molecular masses of species s, t , respectively.

The mixture translational thermal conductivity is determined by:²⁷

$$[K_{tr}]_1 = \sum_s a_s. \quad (9)$$

The quantity a_s is the contribution of each species to the overall mixture translational thermal conductivity and may be determined by solving the following system:²⁷

$$\chi_s = a_s \left\{ \frac{\chi_s}{[\lambda_s]_1} + \sum_{t \neq s} \frac{T\chi_t}{5p\mathcal{D}_{st}} \left(6 \left[\frac{m_s}{(m_s + m_t)} \right]^2 + (5 - 4B_{st}) \left[\frac{m_s}{(m_s + m_t)} \right]^2 + 8 \frac{m_s m_t}{(m_s + m_t)^2} A_{st} \right) \right\} \\ - \chi_s \sum_{t \neq s} a_t \left[\left(T \frac{m_s m_t}{(m_s + m_t)^2} \right) / 5p\mathcal{D}_{st} \right] (11 - 4B_{st} - 8A_{st}). \quad (10)$$

The quantities λ_s and B_{st} in (10) represent the conductivity of species s when pure and the second ratio of collision integrals, respectively, defined as:

$$[\lambda_s]_1 = \frac{25c_v k_b T}{16\Omega_1^2(2)}, \quad (11)$$

$$B_{st} = \frac{5\Omega_{st}^1(2) - \Omega_{st}^1(3)}{5\Omega_{st}^1(1)}, \quad (12)$$

where c_v is the specific heat at constant volume of species s , and p is the pressure of the gas mixture.

The rotational and vibrational conductivities are determined using Eucken's formula, in which it is assumed that the conductivity of the gas is separated into two non-interacting parts, $[K_{tr}]_1$ and K_{int} .²⁷ The internal thermal conductivities are given by:

$$K_{rot} = \sum_{i \in s} \frac{\rho_i c_{v,rot}}{\sum_{j \in t} \chi_j / \mathcal{D}_{ij}}, \quad (13)$$

$$K_{vib} = \sum_{i \in s} \frac{\rho_i c_{v,vib}}{\sum_{j \in t} \chi_j / \mathcal{D}_{ij}}, \quad (14)$$

where ρ_i is the partial density defined as the product of the mixture density, ρ and the species mass fraction, Y_i :

$$\rho_i = \rho Y_i. \quad (15)$$

Finally, the collision integrals involved in computing (5) and (9) and the ratio of collision integrals in (12) can be expressed in terms of the VHS parameters as follows:

$$\Omega_{st}^1(1)|_{VHS} = \frac{\pi}{2} d_{ref}^2 \left(\frac{k_b T}{2\pi m_{st}^*} \right)^{1/2} \left(\frac{T_{ref}}{T} \right)^{\omega-1/2} \left[\frac{\Gamma(7/2 - \omega)}{\Gamma(5/2 - \omega)} \right], \quad (16)$$

$$\Omega_{st}^2(2)|_{VHS} = \frac{\pi}{3} d_{ref}^2 \left(\frac{k_b T}{2\pi m_{st}^*} \right)^{1/2} \left(\frac{T_{ref}}{T} \right)^{\omega-1/2} \left[\frac{\Gamma(9/2 - \omega)}{\Gamma(5/2 - \omega)} \right], \quad (17)$$

$$B_{st}|_{VHS} = \frac{5\Gamma(9/2 - \omega) - \Gamma(11/2 - \omega)}{5\Gamma(7/2 - \omega)}. \quad (18)$$

The collision integrals are expressed according to the VSS collision model as:

$$\Omega_{st}^1(1)|_{VSS} = \left(\frac{2}{\alpha + 1} \right) \Omega_{st}^1(1)|_{VHS}, \quad (19)$$

$$\Omega_{st}^2(2)|_{VSS} = \left[\frac{4\alpha}{(\alpha + 1)(\alpha + 2)} \right] \Omega_{st}^2(2)|_{VHS}. \quad (20)$$

The ratio of collision integrals $B_{st}|_{VSS}$ for the VSS collision model is identical to the expression for $B_{st}|_{VHS}$ given in (18). In (7), the collision integral $\Omega_1^2(2)$ is of the form given in (16) or (19) with $s = t$, and in (16)-(20), $\Gamma(x)$ is the gamma function.

Within DSMC, the VHS and VSS parameters in (16)-(20) are often determined simply as the average values of species s and t (e.g., $d_{ref} = \frac{1}{2}(d_{ref,s} + d_{ref,t})$), regardless of the specific collision partners involved in the collision. The model parameters determined using this approach are herein referred to as *collision-averaged* values. When considering collisions within a gas mixture, however, the VHS and VSS model parameters should be prescribed for each specific collision pairing, rather than using a simple averaging rule for all collision pairs.^{1,28} The model parameters determined with this approach are herein referred to as *collision-specific* values.

The gas mixture considered in the present work is a five-species air ($[N_2, O_2, NO, N, O] \in \mathbb{S}$) equilibrium gas mixture. The conditions considered in this work represent typical boundary layer edge conditions for an Orbiter re-entry trajectory point of Mach 20, which corresponds to a pressure of $2300 Pa$. The temperatures considered in the present work range from $1000 K$ to $5000 K$, which are well within the limits of the transport models considered here. To construct the fitting problem, initial values are prescribed for all VHS and VSS parameters, using either *collision-averaged* or *collision-specific* pairing. The transport coefficients are then computed and collectively expressed in vector form as a function of the VHS or VSS parameters over the desired temperature range according to (1), (5), (9), (13), and (14). Note that while the transport coefficients of mass diffusion, viscosity and thermal conductivity are functions of temperature, the VHS and VSS parameters are not. A second vector comprising the transport properties given by the ‘standard’ SCEBD and Gupta-Yos models is constructed, and the goal of the fitting process is to minimize the distance (or error) between the two vectors by adjusting the VHS or VSS parameters. The adjustment of the VHS/VSS parameters is performed using the Nelder-Mead Simplex Method.^{24,25} This method uses an iterative direct search algorithm to determine the appropriate set of variables required to achieve a minimum difference between the two vectors. The vector of transport coefficients computed from the initial VHS/VSS parameter values forms the first function iteration. The simplex method then perturbs the parameters, and the new transport coefficients are computed and assembled into vector form. If the resulting perturbation produces a smaller distance between the vectors, the simplex method extends the perturbation in the same direction and continues the search. If the perturbation resulted in a larger distance between the two vectors, the simplex method searches in the opposite direction in parameter space.

III. DSMC Particle Generation

Particles generated at a non-equilibrium hybrid interface may be introduced into the computational domain using either a volume reservoir or surface reservoir approach.^{7,14} While these methods have been successfully applied for simple (single-species, monatomic) gases, the current work seeks to extend the reservoir approaches to gas mixtures with internal degrees of freedom. In this section, the perturbation describing the non-equilibrium nature of the gas mixture is derived by way of the Generalized Chapman-Enskog framework, and a sampling procedure is outlined for DSMC particle generation from this non-equilibrium distribution.²⁹

Consider a gas mixture of \mathbb{S} species with internal degrees of freedom inside a reservoir extending from $(-\infty < x \leq 0)$ which is perturbed slightly from the equilibrium Maxwell-Boltzmann distribution. In the Generalized Chapman-Enskog framework, the velocity distribution describing the particle thermal velocities of species s within the reservoir may be expressed as:

$$f_s^{(1)}(\mathbf{C}, \mathcal{E}_{int}) = f_s^{(0)}(\mathbf{C}, \mathcal{E}_{int}) \Gamma_s(\mathbf{C}, \mathcal{E}_{int}), \quad s \in \mathbb{S}, \quad (21)$$

where $f_s^{(0)}(\mathbf{C}, \mathcal{E}_{int})$ is the equilibrium Maxwell-Boltzmann distribution defined by:

$$f_s^{(0)}(\mathbf{C}, \mathcal{E}_{int}) = \left(\frac{\beta}{\pi^{1/2}} \right)^3 \frac{g_{int}}{Z_{int}} \exp \left[-(\beta^2 C_x^2 + \beta^2 C_y^2 + \beta^2 C_z^2) - \mathcal{E}_{int} \right]. \quad (22)$$

Here, $Z_{int} = Z_{rot} Z_{vib}$ is the internal partition function, which can be written as the product of Z_{rot} and Z_{vib} assuming the molecules in the system follow rigid rotator and harmonic oscillator models, and $\mathcal{E}_{int} = \epsilon_{int}/k_b T_{int}$ is the scaled internal energy. In this work, it is assumed that the rotational relaxation occurs rapidly such that $T_{tr} \approx T_{rot}$, resulting in the scaling $\mathcal{E}_{rot} = \epsilon_{rot}/k_b T_{tr}$. Vibrational relaxation processes occur over a much longer timescale, such that $T_{tr} \neq T_{vib}$, resulting in the scaling $\mathcal{E}_{vib} = \epsilon_{vib}/k_b T_{vib}$. Note also that the degeneracy g_{vib} of the harmonic oscillator is unity. In Eq. (21), $\Gamma_s(\mathbf{C}, \mathcal{E}_{int}) = 1 + \phi_{GCE,s}(\mathbf{C}, \mathcal{E}_{int})$ is the perturbation function describing the small departure from the equilibrium state for species s , which may be expressed in terms of the macroscopic fluxes as:

$$\begin{aligned} \Gamma_s(\mathbf{C}, \mathcal{E}_{int}) = & 1 + 2(\mathbb{D}_{x,s} \mathcal{C}_{x,s} + \mathbb{D}_{y,s} \mathcal{C}_{y,s} + \mathbb{D}_{z,s} \mathcal{C}_{z,s}) \\ & + (q_{x,s} \mathcal{C}_{x,s} + q_{y,s} \mathcal{C}_{y,s} + q_{z,s} \mathcal{C}_{z,s}) \left(\frac{2}{5} \mathcal{C}_s^2 - 1 \right) \\ & + (\tilde{q}_{int,x,s} \mathcal{C}_{x,s} + \tilde{q}_{int,y,s} \mathcal{C}_{y,s} + \tilde{q}_{int,z,s} \mathcal{C}_{z,s}) (\mathcal{E}_{int,s} - \bar{\mathcal{E}}_{int,s}) \\ & - 2(\mathcal{C}_{x,s} \mathcal{C}_{y,s} \tau_{xy,s} + \mathcal{C}_{x,s} \mathcal{C}_{z,s} \tau_{xz,s} + \mathcal{C}_{y,s} \mathcal{C}_{z,s} \tau_{yz,s}) \\ & - \mathcal{C}_{x,s}^2 \tau_{xx,s} - \mathcal{C}_{y,s}^2 \tau_{yy,s} - \mathcal{C}_{z,s}^2 \tau_{zz,s}. \end{aligned} \quad (23)$$

The perturbation $\phi_{GCE,s}$ in Eq. (23) is the Generalized Chapman-Enskog (GCE) perturbation, which is written in terms of the dimensionless species diffusion flux, shear stress and heat flux components. As will be shown in Section IV(B), these dimensionless fluxes, or breakdown parameters, can be used as a measure of the non-equilibrium nature of the flowfield, and are demonstrated to provide an indication of the importance of the diffusion and internal heat fluxes on the overall perturbation. The translational heat flux and shear stress components in Eq. (23) are defined for species s :

$$\tau_{ij,s} = \frac{\mu_s}{p_s} \left(\partial_j v_i + \partial_i v_j - \frac{2}{3} \partial_k v_k \delta_{ij} \right) = \frac{\tau_{ij,s}^{NS}}{p_s}, \quad (24)$$

$$q_{i,s} = -\frac{2\beta_s}{p_s} K_s \partial_i T_s = \frac{2\beta_s q_{i,s}^{NS}}{p_s}, \quad (25)$$

and for the gas mixture we introduce the dimensionless diffusion and internal heat flux components defined as:

$$\mathbb{D}_s = \frac{\beta_s \rho_s V_{i,s}}{\rho_s} = \frac{\beta_s D_{i,s}^{NS}}{\rho_s}, \quad (26)$$

$$\tilde{q}_{int,i,s} = -\frac{2\beta_s K_{int,s}}{\rho_s c_{int,s} T_{int,s}} \partial_i T_{int,s} = \frac{2\beta_s q_{int,i,s}^{NS}}{\rho_s c_{int,s} T_{int,s}}, \quad (27)$$

where $D_{i,s}^{NS} = \rho_s V_{i,s}$ is the species diffusion flux, and c_{int} represents the internal (rotational or vibrational) specific heats. The bulk viscosity is excluded in the derivation of the perturbation function. The details of the formulation of $\phi_{GCE,s}$ are provided in Stephani *et al.*²⁹

Particles generated within a volume reservoir may be sampled from the distribution shown in Eq. (21) using an acceptance-rejection procedure outlined at the end of this section. To generate particles using a surface reservoir approach, the particles must be sampled from a distribution which describes the molecules of species s within this reservoir which cross the surface reservoir boundary at $x = 0$ and enter into the computational domain per unit time and area. This is equivalent to determining the ratio of the flux of species s molecules which cross the hybrid surface into the computational domain to the total number of molecules of species s with motion in the $+x$ direction per unit time and area:

$$f_{SR,s}^{(1)}(\mathbf{C}, \mathcal{E}_{int}) d\mathbf{C} = \frac{n(C_x + u_s) f_s^{(1)}(\mathbf{C}, \mathcal{E}_{int}) dC_z dC_y dC_x}{n \int_{-u}^{\infty} \int_{-\infty}^{\infty} \int_{-\infty}^{\infty} (C_x + u_s) f_s^{(1)}(\mathbf{C}, \mathcal{E}_{int}) dC_z dC_y dC_x}. \quad (28)$$

After evaluation of this expression, we arrive at the distribution function for particles of species s generated at a surface reservoir within a non-equilibrium gas mixture:

$$f_{SR,s}^{(1)}(\mathbf{C}, \mathcal{E}_{int}) = f_{SR,s}(C_x) f_{SR,s}(C_y) f_{SR,s}(C_z) \Gamma_s(\mathbf{C}, \mathcal{E}_{int}). \quad (29)$$

We have expressed this distribution as a product of the surface reservoir distributions, defined below, and the corresponding perturbation function given by Eq. (23). The surface reservoir tangential distributions follow regular Maxwellian distributions:

$$f_{SR,s}(C_y, C_z) = \left(\frac{\beta_s}{\pi^{1/2}} \right) \exp \left(-\beta_s^2 C_{(y,z)}^2 \right), \quad (30)$$

while the surface reservoir normal distribution contains the form of the equilibrium one-sided Maxwellian distribution, but is modified by the integration over the perturbation included in (28), and is given as:

$$f_{SR,s}(C_x) = \frac{2\beta_s^2(C_x + u_s) \exp(-\beta_s^2 C_x^2) / (u_s \sqrt{\pi} \beta_s)}{\left\{ 1 + \operatorname{erf}(\beta_s u_s) + \frac{1}{u_s \sqrt{\pi} \beta_s} \exp(-\beta_s^2 u_s^2) + \frac{\mathbb{D}_{x,s}}{u_s \beta_s} [1 + \operatorname{erf}(\beta_s u_s)] \right.} \\ - \frac{q_{x,s}}{5\sqrt{\pi}} \exp(-\beta_s^2 u_s^2) + \frac{\tilde{q}_{int,x,s}(\mathcal{E}_{int,s} - \bar{\mathcal{E}}_{int,s})}{2u_s \beta_s} (1 + \operatorname{erf}(\beta_s u_s)) \\ - \left[\frac{1}{u_s \sqrt{\pi} \beta_s} \exp(-\beta_s^2 u_s^2) + \frac{1}{2} [1 + \operatorname{erf}(\beta_s u_s)] \right] \tau_{xx,s} \\ - \frac{1}{2} \left[\frac{1}{u_s \sqrt{\pi} \beta_s} \exp(-\beta_s^2 u_s^2) + [1 + \operatorname{erf}(\beta_s u_s)] \right] \tau_{yy,s} \\ \left. - \frac{1}{2} \left[\frac{1}{u_s \sqrt{\pi} \beta_s} \exp(-\beta_s^2 u_s^2) + [1 + \operatorname{erf}(\beta_s u_s)] \right] \tau_{zz,s} \right\}. \quad (31)$$

Particles are generated from the volume reservoir distribution (Eq. (21)) or the surface reservoir distribution (Eq. (29)) following an approach similar to that for the simple gas, however the distribution for the gas mixture is computed specifically for each species according to the species-specific flux information provided by the Navier-Stokes solution. The perturbation function is now dependent on the particle internal energy as well as the thermal velocity, thus the rotational and vibrational internal energy levels must be determined for each particle before the perturbation function can be completely specified. It is also important to note that the non-equilibrium distribution for a gas mixture with internal energy is prescribed by a perturbation of the Maxwell-Boltzmann distribution (Eq. (22)). This perturbation therefore describes not only the non-equilibrium nature of the velocity distribution functions, but also the non-equilibrium nature of the internal energy distribution functions, according to the macroscopic flux quantities comprising the perturbation in Eq. (23). In order to sample this distribution, both the thermal velocities and internal energies are included in the acceptance/rejection step, thereby ‘filtering’ these sampled quantities to reflect the non-equilibrium nature of the flow (see Figure 1).

To generate particle thermal velocities and internal energies from the non-equilibrium distributions in Eq. (21) or Eq. (29), we use the following acceptance-rejection algorithm:

IV. Results

A. Comparison of CFD and fitted DSMC transport properties

1. VHS: Collision-averaged and collision-specific pairing

The results from the fitting of the transport coefficients determined by the VHS collision model are presented in Figures 2-4. The transport coefficients produced by the SCEBD and Gupta-Yos transport models are shown in Figures 2(a)-4(a) (solid lines) as a function of temperature. For comparison, these figures also include the corresponding DSMC transport coefficients (dashed lines), which are computed based on the fitted *collision-averaged* parameters obtained from the Nelder-Mead algorithm.

The results obtained from the fitting process are shown in Figures 2(b)-4(b) and 2(c)-4(c) for the *collision-averaged* and *collision-specific* pairing approaches, respectively, and are expressed in terms of percent error. These errors represent the difference in the DSMC transport properties from the CFD (SCEBD/Gupta-Yos) transport coefficients, normalized by the CFD transport coefficient value and presented as a percentage. The VHS model parameters considered in the fitting process include the reference diameter, d_{ref} , and temperature exponent, ω . This results in a total of ten variable parameters in the *collision-averaged* approach or thirty variable parameters in the *collision-specific* approach.

The VHS collision model is found to provide reasonable agreement with the CFD models for diffusion, viscosity and thermal conductivity, but as shown in Figures 2-4, this model is only capable of producing fitted mixture transport coefficients that lie within 15% – 20% of the SCEBD and Gupta-Yos model values. The fitting of the VHS parameters result in DSMC diffusion coefficients that lie within 15% of the CFD diffusion coefficients determined from the SCEBD model, using both collision-averaged and collision-specific pairing (Figures 2(b,c)). The collision-specific pairing performs particularly well over the temperature range of 1000K – 4000K, while the collision-averaged pairing shows noticeable errors over the entire temperature range. Similar trends are observed in the errors in the mixture viscosity (Figures 3(b,c)) and the translational, rotational and vibrational thermal conductivities (Figures 4(b,c)). The collision-specific pairing approach offers a slight advantage over the collision-averaged pairing, and this is likely due to the fact that more variables are available in the collision-specific fitting process. The best-fit VHS parameter values are tabulated in Appendix B.

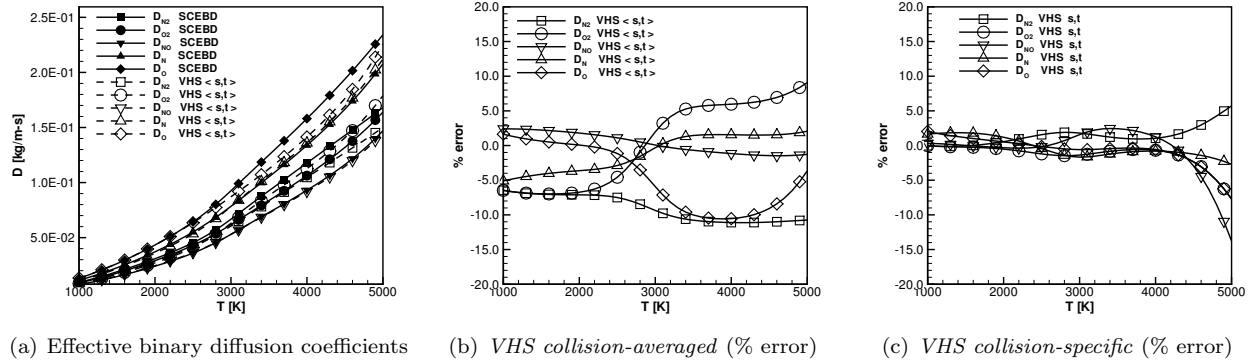


Figure 2. (a) Comparison of effective binary diffusion coefficients for five-species air, computed from fitted VHS collision-averaged pairing approach (dashed lines with open symbols) and SCEBD model (solid lines with closed symbols). Percent error of fitted VHS collision-averaged (b) and collision-specific (c) effective diffusion coefficients relative to SCEBD model.

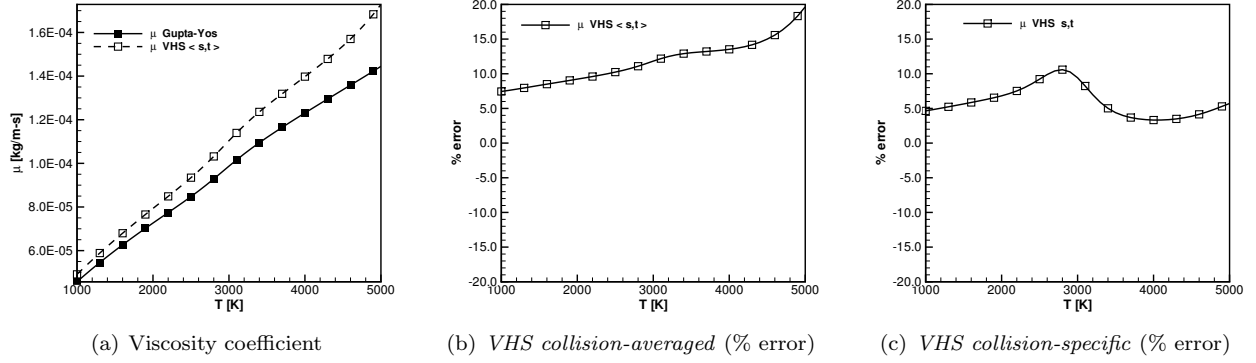


Figure 3. (a) Comparison of viscosity coefficient for five-species air, computed from fitted VHS collision-averaged pairing approach (dashed line with open symbols) and Gupta-Yos model (solid line with closed symbols). Percent error of fitted VHS collision-averaged (b) and collision-specific (c) viscosity coefficient relative to Gupta-Yos model.

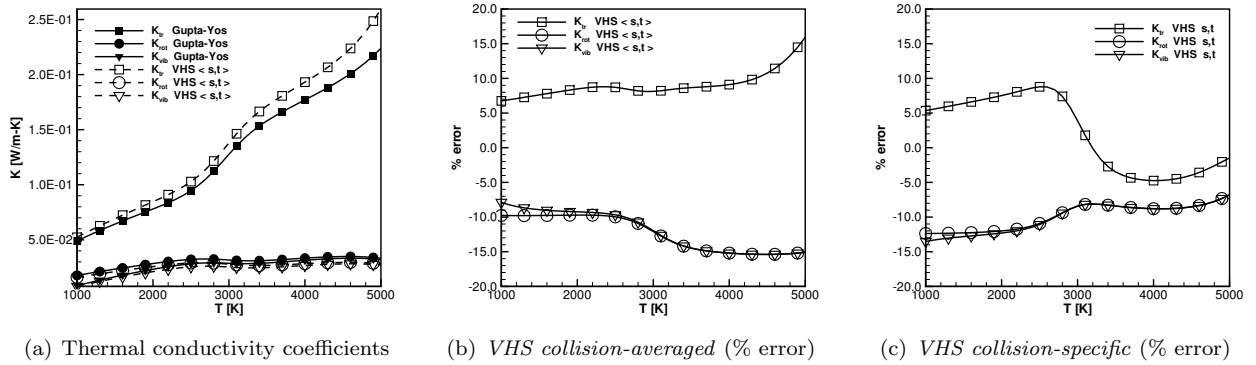


Figure 4. (a) Comparison of thermal conductivity coefficients for five-species air, computed from fitted VHS collision-averaged pairing approach (dashed lines with open symbols) and Gupta-Yos model (solid lines with closed symbols). Percent error of fitted VHS collision-averaged (b) and collision-specific (c) thermal conductivity coefficients relative to Gupta-Yos model.

2. VSS: Collision-averaged and collision-specific pairing

The results from the fitting of the transport coefficients determined by the VSS collision model are presented in Figures 5-7. The transport coefficients produced by the SCEBD and Gupta-Yos transport models are again shown in Figures 5(a)-7(a) (solid lines), along with the fitted VSS *collision-averaged* transport coefficients (dashed lines) as a function of temperature.

The results obtained from the fitting process are shown in Figures 5(b)-7(b) and 5(c)-7(c) for the VSS *collision-averaged* and *collision-specific* pairing approaches, respectively. The VSS model parameters considered in the fitting process include the reference diameter, d_{ref} , and temperature exponent, ω and VSS exponent, α . This results in a total of fifteen variable parameters in the *collision-averaged* approach or forty-five variable parameters in the *collision-specific* approach.

The VSS collision model is found to provide exceptional agreement with the CFD models for diffusion, viscosity and thermal conductivity. The fitting results in Figures 5-7 indicate that this model is capable of producing fitted mixture transport coefficients that lie within 5% of the SCEBD and Gupta-Yos model values. The fitting of the VSS parameters result in DSMC diffusion coefficients that lie within 5% of the CFD diffusion coefficients determined from the SCEBD model using the collision-averaged pairing (Figure 5(b)), while the error using the collision-specific pairing (Figures 5(c)) remains within 3%. Similar trends are observed in the errors in the mixture viscosity (Figures 6(b,c)) and the translational, rotational and vibrational thermal conductivities (Figures 7(b,c)). The collision-specific pairing approach offers a slight advantage over the collision-averaged pairing, and again, this is likely due to the fact that more variables are available in the collision-specific fitting process. However, it is important to note that the choice of collision cross-section model has a greater impact on the overall agreement achieved in the transport coefficient fits. The collision pairing approach (i.e., collision-averaged versus collision-specific) should only be a secondary consideration when determining the best-fit collision model parameters. The best-fit VSS parameter values are also tabulated in Appendix B.

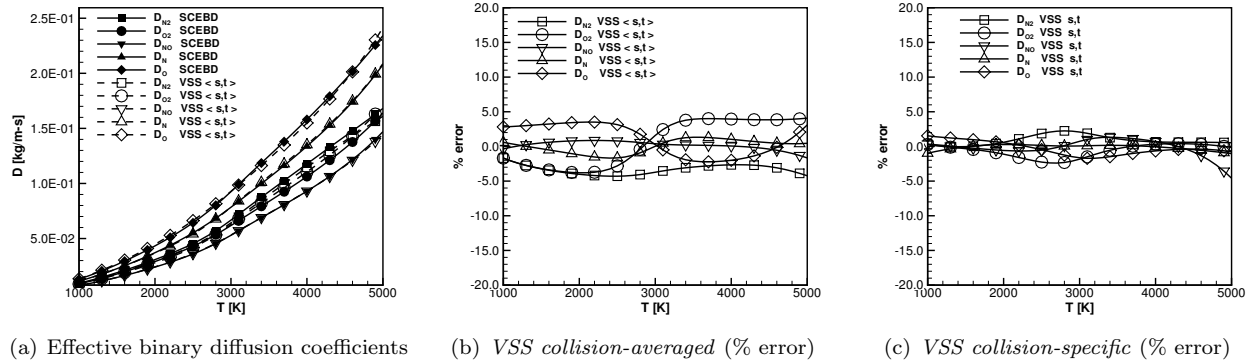


Figure 5. (a) Comparison of effective binary diffusion coefficients for five-species air, computed from fitted VSS collision-averaged pairing approach (dashed lines with open symbols) and SCEBD model (solid lines with closed symbols). Percent error of fitted VSS collision-averaged (b) and collision-specific (c) effective diffusion coefficients relative to SCEBD model.

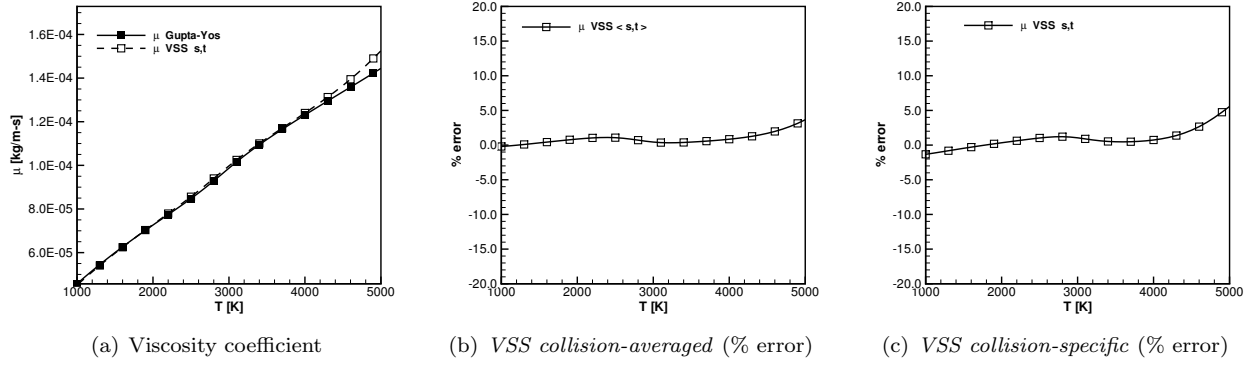


Figure 6. (a) Comparison of viscosity coefficient for five-species air, computed from fitted VSS collision-specific pairing approach (dashed line with open symbols) and Gupta-Yos model (solid line with closed symbols). Percent error of fitted VSS collision-averaged (b) and collision-specific (c) viscosity coefficient relative to Gupta-Yos model.

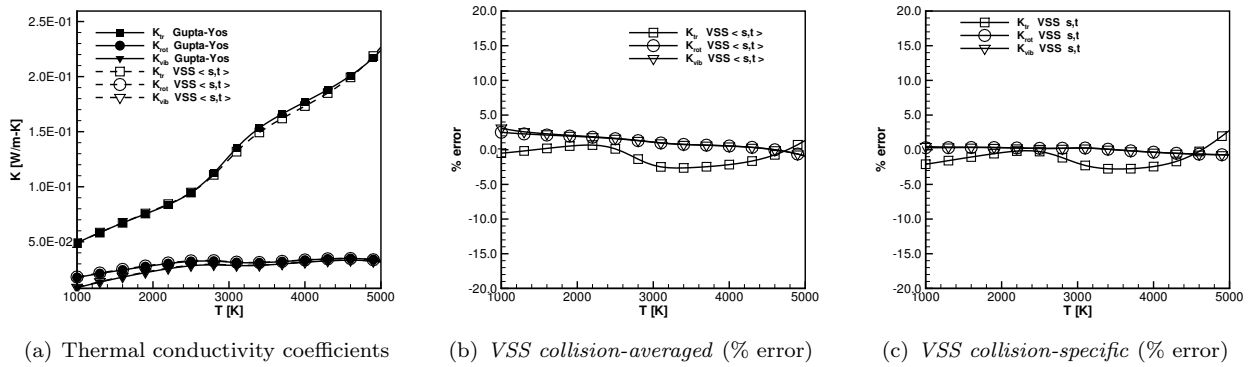


Figure 7. (a) Comparison of thermal conductivity coefficients for five-species air, computed from fitted VSS collision-averaged pairing approach (dashed lines with open symbols) and Gupta-Yos model (solid lines with closed symbols). Percent error of fitted VSS collision-averaged (b) and collision-specific (c) thermal conductivity coefficients relative to Gupta-Yos model.

B. Evaluation of the breakdown parameters in a five-species air gas mixture

In this section, we present a simple analysis to assess the importance of the additional diffusion and internal heat flux terms that are introduced through the formulation of the Generalized Chapman-Enskog perturbation. The analysis that is outlined in this section is applied to CFD solutions of two general flow cases, but this analysis can be easily extended to any Navier-Stokes flowfield solution to determine (a) where the Navier-Stokes solution breaks down (spatially), and (b) the macroscopic flux parameter(s) that lead to breakdown, according to the breakdown criterion of $B \leq 0.1$ suggested for Chapman-Enskog particle generation.¹⁴ Finally, this analysis can be used to determine whether DSMC particles may be generated from the regular Chapman-Enskog distribution (in cases where diffusion or internal heat flux contributions are negligible), or if the Generalized Chapman-Enskog distribution is required. To demonstrate this analysis, we evaluate the relative sizes of each of the breakdown parameters in two types of flows: (1) hypersonic flat-plate boundary layer flow, and (2) the breakdown region near a shock formed by two-dimensional hypersonic flow over a cylinder.

In each of these cases, we consider a reacting five-species air gas mixture, with the freestream conditions shown in Table 1. In both cases, the flat plate and cylinder surfaces are treated as non-catalytic, isothermal walls (where $T_w = 1000K$), and a no-slip wall condition is enforced. The flowfields are computed using DPLR,³⁰ in which reactions are computed using Park's finite-rate chemistry model.³¹ The flow is modeled allowing for translational, rotational and vibrational thermal non-equilibrium, and the mixture transport coefficients (diffusion, viscosity and thermal conductivities) are computed using the self-consistent effective binary diffusion (SCEBD) and Gupta-Yos models.^{21,22} Note that the SCEBD model uses a mixing rule to approximate the effective diffusion coefficient of each species s in the gas mixture, while the Gupta-Yos model computes mixture viscosity and thermal conductivities. Therefore, in the analysis of the cases that follow, the flux parameters (given by (24) - (27)) and perturbations (ϕ_{CE}^{14} and $\phi_{GCE,s}$ from (23)) are determined using *species-specific* diffusion fluxes and *mixture* shear stress and heat fluxes that are output from the DPLR solution.

Table 1. Freestream Conditions

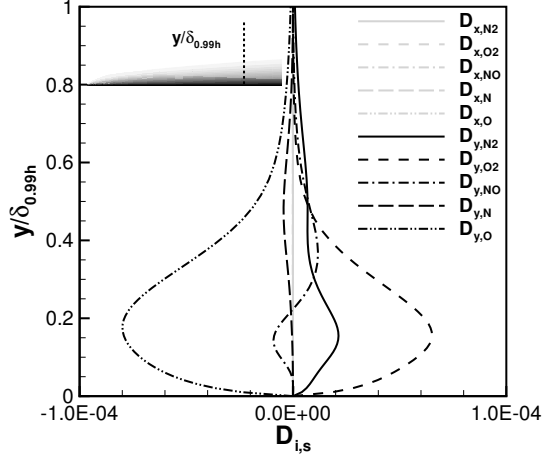
	Flat Plate (boundary layer)	Cylinder (normal shock)
M	3.0	11.4
p	2100 Pa	52 Pa
T	4000 K	265 K
u	4100 m/s	3740 m/s
χ_{N_2}	6.04×10^{-1}	7.9×10^{-1}
χ_{O_2}	1.0×10^{-3}	2.1×10^{-1}
χ_{NO}	7.0×10^{-3}	—
χ_N	8.0×10^{-3}	—
χ_O	3.80×10^{-1}	—

1. Hypersonic 2-D boundary layer flow

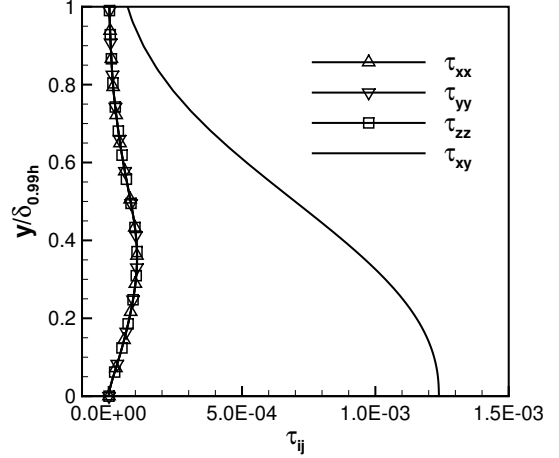
The breakdown parameters from the flat-plate boundary layer flow case are presented in Figure 8. The diffusion, shear stress and heat flux breakdown parameters were computed according to (24)-(27), using either species-specific or mixture quantities as stated previously. The breakdown parameters are plotted as a function of wall-normal distance, normalized by the boundary layer thickness, $\delta_{0.99h}$, as indicated schematically in Figure 8(a). The boundary layer thickness was determined as the location above the surface where the enthalpy had recovered to 99% of the freestream value.

In Figure 8(a), the diffusion breakdown parameter is plotted for each species s , and for each flux direction (x, y) in the boundary layer flow. The diffusion flux computed in DPLR is determined for gradients in concentration only, while the thermal diffusion (flux due to gradients in temperature) is neglected. Note that the diffusion fluxes due to streamwise concentration gradients ($\mathbb{D}_{x,s}$) are all essentially zero. The diffusion fluxes

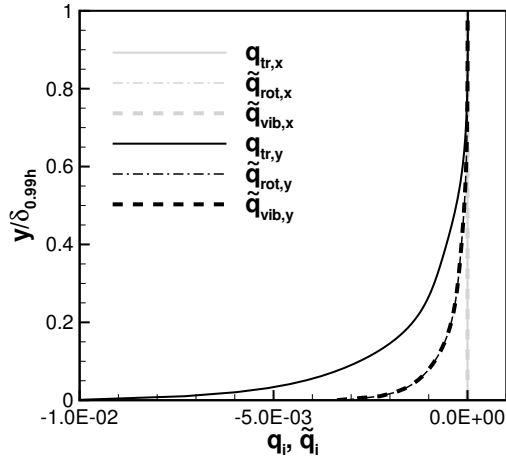
due to wall-normal concentration gradients ($\mathbb{D}_{y,s}$) are largest near the wall, with maximum values observed at approximately $0.2\delta_{0.99h}$. The strongest diffusion occurs for the atomic oxygen and molecular oxygen, and all diffusion fluxes decay towards zero approaching the boundary layer edge. The magnitudes of the diffusion breakdown parameters are relatively small in comparison to the shear stress breakdown parameters, shown in Figure 8(b). The relevant stress tensor quantities in this two-dimensional boundary layer flow are the normal stress components, τ_{xx} , τ_{yy} , τ_{zz} and the shear stress component τ_{xy} , while the remaining stress tensor components are zero. The maximum values of the normal stress breakdown parameters are comparable in magnitude to the diffusion breakdown parameters, but the shear stress breakdown parameter is an order of magnitude larger, with a maximum value at the wall of approximately 1.25×10^{-3} .



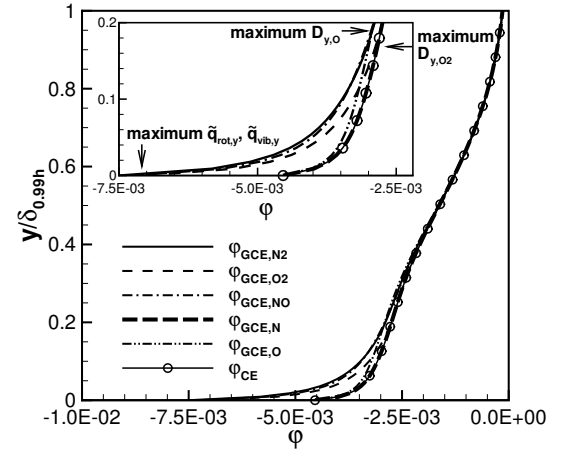
(a) Diffusion breakdown parameter, $\mathbb{D}_{i,s}$ (per flux direction, per species) through boundary layer.



(b) Shear stress breakdown parameter, τ_{ij} (per tensor component) through boundary layer.



(c) Heat flux breakdown parameter, q_i , \tilde{q}_i (per mode, per flux direction) through boundary layer.



(d) Comparison of perturbation, $\phi_{GCE,s}$ (Generalized Chapman-Enskog (GCE) per species), ϕ_{CE} (Chapman-Enskog (CE)) through boundary layer.

Figure 8. Breakdown parameters (a) $\mathbb{D}_{i,s}$, (b) τ_{ij} , (c) q_i , \tilde{q}_i through a hypersonic 2-D boundary layer in five-species air, plotted as a function of wall-normal distance (shown schematically in the inset figure of (a)). (d) Comparison of perturbation ϕ computed using Chapman-Enskog (CE) formulation¹⁴ or Generalized Chapman-Enskog (GCE) formulation for each species (Equation (23)).

The heat flux breakdown parameters are provided in Figure 8(c) as a function of wall-normal distance. The parameters in the figure represent the translational, rotational and vibrational heat fluxes due to stream-

wise and wall-normal temperature gradients. Note again that the streamwise component of the heat flux breakdown parameters are essentially zero, as shown for $q_{tr,x}$, $\tilde{q}_{rot,x}$, and $\tilde{q}_{vib,x}$. Each of the wall-normal heat flux breakdown parameters have maximum values at the wall, and it is observed that for this boundary layer flow solution, $q_{tr,y}$ provides the largest contribution to the non-equilibrium perturbation up to a distance of approximately $0.4\delta_{0.99h}$. It is also important to note that the internal heat flux breakdown parameters are approximately the same magnitude as the shear stress breakdown parameter throughout the boundary layer, which suggests the importance of including the internal energy contributions in determining the non-equilibrium velocity distribution function.

To assess the significance of these breakdown parameters, we use the breakdown parameter profiles provided in Figure 8(a)-(c), as well as the local flowfield information, to approximate the perturbation ϕ in the boundary layer according to the Generalized Chapman-Enskog formulation $\phi_{GCE,s}$ (23) and the Chapman-Enskog formulation ϕ_{CE} .¹⁴ The particle thermal velocity and the particle internal energies are approximated by their most probable values, and so \mathcal{C}_i and \mathcal{E}_{int} in these expressions take on values of unity for purposes of this approximation. The purpose of this comparison between the perturbations ϕ_{GCE} and ϕ_{CE} is to understand the overall effect of the additional diffusion and internal heat flux contributions on the calculation of the perturbed distribution function. The resulting profiles are shown in Figure 8(d). The perturbations computed from the Generalized Chapman-Enskog formulation for each of the five species are represented by the solid and broken lines, and are plotted as a function of wall-normal distance. The solid line with an open circle symbol represents the perturbation computed from the regular Chapman-Enskog formulation. Several observations can be made from the comparison of these perturbations. First, it is seen that the perturbations are nearly indistinguishable in the outer part of the boundary layer, for $0.4 < y/\delta_{0.99h}$. It is also observed that the perturbation $\phi_{GCE,N}$ for atomic nitrogen follows the Chapman-Enskog perturbation ϕ_{CE} almost perfectly, which is consistent with the fact that the diffusion flux of atomic nitrogen is very small throughout the boundary layer, as shown in Figure 8(a). The perturbation $\phi_{GCE,O}$ of atomic oxygen, on the other hand, is seen to deviate slightly from ϕ_{CE} by approximately 5% at a distance $0.2\delta_{0.99h}$, which corresponds to the location of maximum diffusion flux $\mathbb{D}_{y,O}$ in the boundary layer.

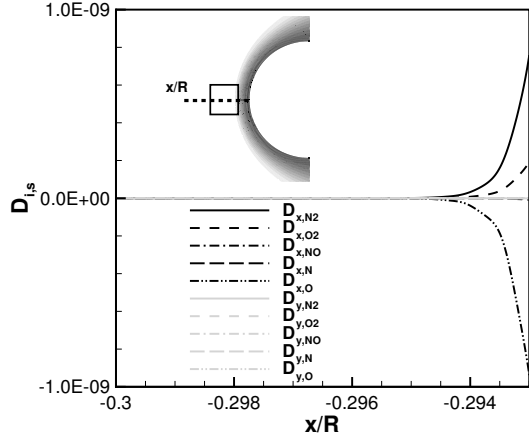
The comparison of the perturbations ϕ_{GCE} and ϕ_{CE} for the molecular species N_2 , O_2 and NO show considerable differences near the wall (Figure 8(d), enlarged inset figure), which can be attributed to the inclusion of the internal heat flux in the calculation of the perturbation ϕ_{GCE} . The magnitude of the Generalized Chapman-Enskog perturbation at the wall is approximately 30 – 40% larger than the perturbation predicted by the Chapman-Enskog formulation. The perturbation ϕ_{GCE,O_2} of molecular oxygen is driven towards the Chapman-Enskog perturbation ϕ_{CE} for wall-normal distances greater than $0.2\delta_{0.99h}$, which corresponds to the large positive diffusion flux observed in this region in Figure 8(a). Approaching the wall, however, the heat flux contribution dominates the perturbation, and the perturbation ϕ_{GCE,O_2} follows the asymptotic trend of the other molecular constituents (molecular nitrogen and nitric oxide) toward the wall. Note that the diffusion flux breakdown parameters of molecular nitrogen and nitric oxide are comparatively small throughout the boundary layer. It should also be noted that although the perturbation ϕ_{GCE} becomes considerably larger than ϕ_{CE} near the wall, the magnitude of the breakdown parameters are less than 0.1 throughout the boundary layer, and thus Generalized Chapman-Enskog Theory is still expected to adequately represent the perturbation of the velocity distribution function.¹⁴

2. Hypersonic flow over a cylinder (normal shock flow)

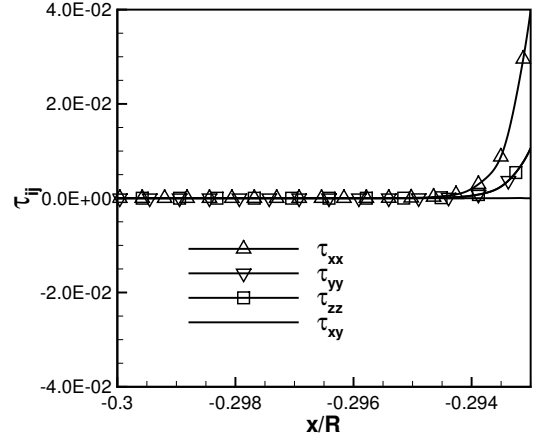
The breakdown parameters from the hypersonic flow over a cylinder are shown in Figure 9 as a function of the distance along the stagnation line x/R , where the cylinder surface is located at $x/R = 0$, and the shock is located at $x/R \approx -0.289$. The diffusion flux, shear stress and heat flux breakdown parameters are computed in the same way as discussed in Section IV(B.1). Unlike the boundary layer flow case, the gradients within the normal shock become large very quickly, and the breakdown criterion is exceeded by the parameters at various x/R locations. To present the results from this analysis, we only show the breakdown parameter profiles up to the x/R location where the first parameter exceeds the breakdown criterion, $B \leq 0.1$. This region is upstream of the normal shock, and is represented schematically in the inset figure of Figure 9(a). As will be shown, the translational heat flux parameter exceeds this breakdown criterion first, at a location of approximately $x/R = -0.293$. After this point (for larger values of x/R), the approximations used to formulate the perturbation become invalid.

The diffusion flux breakdown parameters are shown in Figure 9(a) per flux direction and per species. Although the diffusion fluxes become larger within the shock and shock layer, they are completely negligible

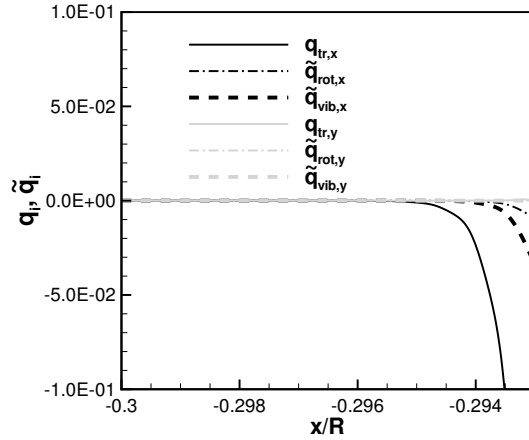
within the breakdown region presented here. This observation, as well as the resulting analysis of the boundary layer flow, suggests that the mass diffusion flux plays a relatively minor role in the total perturbation of the velocity distribution function. It is important to note, however, that the present formulation of the Generalized Chapman-Enskog perturbation neglects terms which arise due to chemical reactions, in which diffusion mechanisms may become relatively important.



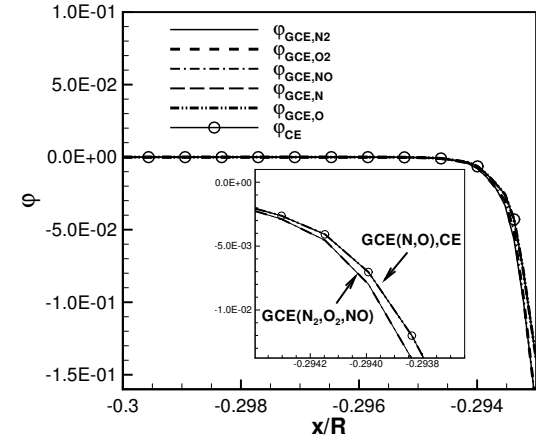
(a) Diffusion breakdown parameter, $\mathbb{D}_{i,s}$ (per flux direction, per species) along stagnation line, up to breakdown location.



(b) Shear stress breakdown parameter, τ_{ij} (per tensor component) along stagnation line, up to breakdown location.



(c) Heat flux breakdown parameter, q_i , \tilde{q}_i (per mode, per flux direction) along stagnation line, up to breakdown location.



(d) Comparison of perturbation, $\phi_{GCE,s}$ (Generalized Chapman-Enskog (GCE) per species), ϕ_{CE} (Chapman-Enskog (CE)) along stagnation line, up to breakdown location.

Figure 9. Breakdown parameters (a) $\mathbb{D}_{i,s}$, (b) τ_{ij} , (c) q_i , \tilde{q}_i along the stagnation streamline, plotted as a function of streamwise distance in the breakdown region upstream of a normal shock (shown schematically in the inset figure of (a)). (d) Comparison of perturbation ϕ computed using Chapman-Enskog (CE) formulation¹⁴ or Generalized Chapman-Enskog (GCE) formulation (Equation (23)).

The stress tensor breakdown parameters are shown in Figure 9(b). In this case, the normal stresses increase appreciably before the breakdown location, with $\tau_{xx} = 4.0 \times 10^{-2}$ and $\tau_{yy}, \tau_{zz} = 1.0 \times 10^{-2}$, while the shear stress parameter remains negligible, in contrast to the boundary layer flow case. The translational, rotational and vibrational heat flux parameters are presented next in Figure 9(c). The translational heat flux is the first parameter to exceed the breakdown criterion, with $|q_{tr}| = 0.1$ at a location of $x/R = -0.2935$. The values of the rotational and vibrational heat flux parameters, which lag the translational contribution, are also observed to increase before the breakdown location.

The dominance of this translational heat flux is evident in the total perturbation, plotted in Figure 9(d) as a function of distance x/R . In this figure, we have again computed the perturbation from the General-

ized Chapman-Enskog formulation which includes the contributions from the diffusion fluxes and internal heat fluxes on the total perturbation of the velocity distribution function. The curves representing the perturbation $\phi_{GCE,s}$ of the atomic species N, O are indistinguishable from the regular Chapman-Enskog perturbation; this underscores the fact that the diffusion flux has no effect on the total perturbation for this flow case. The curves representing the perturbation of the molecular species do deviate slightly from the regular Chapman-Enskog perturbation, due to the influence of the internal heat fluxes on the total perturbation, but this difference ($\approx 2\%$) is negligible in comparison to the boundary layer flow case. As indicated by the breakdown parameters in this analysis, it would be necessary to generate the surface reservoir at the breakdown location of $x/R \approx -0.293$. It is seen that the regular Chapman-Enskog perturbation ϕ_{CE} adequately represents the total perturbation, and the use of the Generalized Chapman-Enskog perturbation is unnecessary for the normal shock flow conditions considered here.

V. Conclusion

A general approach for achieving consistency in the species diffusion, viscosity and thermal conductivity coefficients between DSMC and CFD (Navier-Stokes) solvers was presented for a five-species air gas mixture. The CFD transport coefficients were considered as the ‘standard’ values to which the DSMC transport coefficients were fitted by selectively adjusting the VHS/VSS parameters using the Nelder-Mead Simplex Method. Through this process, it was determined that it is more important to use the appropriate (VSS) collision model in a DSMC simulation involving gas mixtures in order to match all transport coefficients. The way that the collision model parameters are calculated for a colliding pair (e.g., collision-averaged or collision-specific) should be a secondary consideration when determining collision model parameters.

A new method for DSMC particle generation at non-equilibrium hybrid interfaces involving gas mixtures with internal energy was also presented. The perturbation describing the non-equilibrium distribution function was expressed in terms of Navier-Stokes flux quantities including species diffusion, shear stress, and translational and internal heat fluxes. Particle thermal velocity components and internal energies generated at this interface are sampled from this distribution according to the algorithm provided in Section III. The Generalized Chapman-Enskog distribution therefore describes not only the non-equilibrium nature of the velocity distribution functions, but also the non-equilibrium nature of the internal energy distribution functions. This formulation provides a complete set of breakdown parameters, and a simple analysis was presented to assess the significance of the species diffusion and internal energy fluxes in non-equilibrium boundary layer flow and normal shock flow.

Future work will aim to extend these hybrid approaches to include chemical reactions in the formulation of the hybrid interface boundary condition. Other high-enthalpy effects will also be incorporated into this hybrid framework, such as the consideration of weakly-ionized flows.

Acknowledgments

This work was funded by the NASA NRA under contract agreement NNX08AB27A with monitor Dr. Deepak Bose. Computational resources and technical support were provided by TACC at The University of Texas at Austin.

Appendix A: Sampling surface reservoir distributions

The evaluation of the non-equilibrium distribution functions for the surface reservoir in a gas mixture with internal energy (29) results in velocity distribution functions describing the tangential and normal thermal velocity components of particles entering the computational domain. The tangential components in both cases are described as usual by regular Maxwellian distributions, and velocity components ($\mathcal{C}_y, \mathcal{C}_z$) may be sampled from this distribution using the Box-Muller method.^{1,32}

To sample the distributions describing the normal thermal velocity component, we use an acceptance-rejection approach on the distributions shown in (31). An efficient acceptance-rejection sampling on (31) is formulated by normalizing this distribution by its maximum value $f_{SR}(C_{x,MAX})$, where $(C_{x,MAX})$ is determined by solving the following for C_x :

$$\begin{aligned}
\frac{d f_{sR}(C_x)}{d C_x} = & \frac{2\beta_s^2 \exp(-\beta_s^2 C_x^2) - 4\beta_s^4 C_x^2 \exp(-\beta_s^2 C_x^2) - 4\beta_s^4 C_x u \exp(-\beta_s^2 C_x^2)}{(u_s \sqrt{\pi} \beta_s) \left\{ 1 + \operatorname{erf}(\beta_s u_s) + \frac{1}{u_s \sqrt{\pi} \beta_s} \exp(-\beta_s^2 u_s^2) + \frac{\mathbb{D}_{x,s}}{u_s \beta_s} [1 + \operatorname{erf}(\beta_s u_s)] \right.} \\
& - \frac{q_{x,s}}{5\sqrt{\pi}} \exp(-\beta_s^2 u_s^2) + \frac{\tilde{q}_{int,x,s}(\mathcal{E}_{int,s} - \bar{\mathcal{E}}_{int,s})}{2u_s \beta_s} (1 + \operatorname{erf}(\beta_s u_s)) \\
& - \left[\frac{1}{u_s \sqrt{\pi} \beta_s} \exp(-\beta_s^2 u_s^2) + \frac{1}{2} [1 + \operatorname{erf}(\beta_s u_s)] \right] \tau_{xx,s} \\
& - \frac{1}{2} \left[\frac{1}{u_s \sqrt{\pi} \beta_s} \exp(-\beta_s^2 u_s^2) + [1 + \operatorname{erf}(\beta_s u_s)] \right] \tau_{yy,s} \\
& \left. - \frac{1}{2} \left[\frac{1}{u_s \sqrt{\pi} \beta_s} \exp(-\beta_s^2 u_s^2) + [1 + \operatorname{erf}(\beta_s u_s)] \right] \tau_{zz,s} \right\} = 0, \tag{33}
\end{aligned}$$

$$C_{x,MAX} = \frac{\sqrt{(\beta_s u_s)^2 + 2} - \beta_s u_s}{2\beta_s}. \tag{34}$$

The resulting normalized distribution is thus:

$$\frac{f_{sR}(C_x)}{f_{sR}(C_{x,MAX})} = \frac{2\beta_s(C_x + u_s) \exp\left(\frac{1}{2} + \frac{\beta_s u_s}{2} \left(\beta_s u_s - \sqrt{(\beta_s u_s)^2 + 2}\right) - \beta_s^2 C_x^2\right)}{\sqrt{2 + (\beta_s u_s)^2} + \beta_s u_s}. \tag{35}$$

Note that since the terms in the denominator of (33) are independent of C_x , they simply scale the distribution and cancel in the normalization, thus the result in (35) is the same distribution used in the well-established sampling process for the equilibrium normal velocity component.¹

Appendix B: Fitted VHS/VSS collision model parameters

Table 2. Five-Species Air Collision-Averaged VHS/VSS Parameters

VHS	$d_{ref}[\text{\AA}]$	ω	VSS	$d_{ref}[\text{\AA}]$	ω	α
N_2	3.240	0.680	N_2	3.255	0.685	1.444
O_2	2.108	0.734	O_2	2.374	0.680	1.156
NO	2.664	0.724	NO	3.000	0.778	1.118
N	2.249	0.780	N	2.402	0.689	1.088
O	1.645	0.711	O	2.108	0.780	1.686

Table 3. Five-Species Air Collision-Specific VHS/VSS Parameters

VHS						VSS					
$d_{ref}[\text{\AA}]$	N_2	O_2	NO	N	O	$d_{ref}[\text{\AA}]$	N_2	O_2	NO	N	O
N_2	3.153	2.579	2.711	2.422	2.304	N_2	3.387	2.621	2.673	2.615	2.460
O_2		4.082	3.396	2.998	2.409	O_2		2.719	3.738	2.485	2.330
NO			2.203	3.665	2.671	NO			1.532	2.849	3.101
N				2.633	2.733	N				2.680	2.358
O					3.515	O					2.354
ω	N_2	O_2	NO	N	O	ω	N_2	O_2	NO	N	O
N_2	0.686	0.719	0.712	0.731	0.701	N_2	0.683	0.710	0.696	0.730	0.720
O_2		0.683	0.680	0.682	0.708	O_2		0.709	0.699	0.744	0.692
NO			0.681	0.682	0.727	NO			0.694	0.770	0.775
N				0.750	0.718	N				0.689	0.710
O					0.687	O					0.708
α	N_2	O_2	NO	N	O	α	N_2	O_2	NO	N	O
N_2						N_2	1.596	1.063	1.119	1.015	1.238
O_2						O_2		1.030	1.022	1.006	1.004
NO						NO			1.011	1.021	1.143
N						N				1.018	1.019
O						O					1.022

References

- ¹Bird, G., *Molecular Gas Dynamics and the Direct Simulation of Gas Flows*, Oxford University Press, Oxford, 1994.
- ²Hash, D. and Hassan, H., "Assessment of Schemes for Coupling Monte Carlo and Navier-Stokes Solution Methods," *Journal of Thermophysics and Heat Transfer*, Vol. 10, No. 2, April-June, 1996.
- ³Roveda, R., Goldstein, D. B., and Varghese, P. L., "Hybrid Euler/particle approach for continuum/rarefied flows," *Journal of Spacecraft and Rockets*, Vol. 35, No. 3, 1998.
- ⁴Schwartzentruber, T., Scalabrin, L., and Boyd, I., "Hybrid Particle-Continuum Simulations of Hypersonic Flow over a Hollow Cylinder-Flare Geometry," *AIAA Journal* Vol. 46, No. 8 pp 2086-2095, 2008.
- ⁵Schwartzentruber, T., Scalabrin, L., and Boyd, I., "Hybrid Particle-Continuum Simulations of Nonequilibrium Hypersonic Blunt-Body Flowfields," *Journal of Thermophysics and Heat Transfer*, Vol. 22, No.1, 2008.
- ⁶Schwartzentruber, T., Scalabrin, L., and Boyd, I., "Multiscale Particle-Continuum Simulations of Hypersonic Flow over a Planetary Probe," *Journal of Spacecraft and Rockets*, Vol. 45, No. 6, pp 1196-1206, 2008.
- ⁷Schwartzentruber, T., Scalabrin, L., and Boyd, I., "A modular particle-continuum numerical method for hypersonic non-equilibrium gas flows," *Journal of Computational Physics*, Vol. 225, Issue 1, pp 1159-1174, 2007.
- ⁸Roveda, R., Goldstein, D. B., and Varghese, P. L., "Hybrid Euler/direct simulation Monte Carlo calculation for unsteady slit flow," *Journal of Spacecraft and Rockets*, Vol. 37, No. 6, 2000.
- ⁹Deschenes, T. R. and Boyd, I. D., "Application of a Modular Particle-Continuum Method to Partially Rarefied, Hypersonic Flow," *27th International Symposium on Rarefied Gas Dynamics*, 2011.
- ¹⁰Boyd, I., Chen, G., and Candler, G., "Predicting Failure of the Continuum Fluid Equations in Transitional Hypersonic Flows," *Physics of Fluids*, Vol. 7, No. 1, pp 210-219, 1995.
- ¹¹Gallis, M., Torczynski, J., and Rader, D., "Molecular gas dynamics observations of Chapman-Enskog behavior and departures therefrom in nonequilibrium gases," *Physical Review E*, Vol. 69, 2004.
- ¹²Chigullapalli, S., Venkatramana, A., Ivanov, M., and Alexeenko, A., "Entropy considerations in numerical simulations of non-equilibrium rarefied flows," *Journal of Computational Physics*, Vol. 229, Issue 6, 2010.
- ¹³Camberos, J., Schrock, C., McMullan, R., and Branam, R., "Development of Continuum Onset Criteria with Direct Simulation Monte-Carlo Using Boltzmann's H-Theorem: Review and Vision," *AIAA Paper No. 2006-2942*, 2006.
- ¹⁴Garcia, A. and Alder, W., "Generation of the Chapman-Enskog Distribution," *Journal of Computational Physics* 140 66, 1998.
- ¹⁵Brun, R., "Transport Properties in Reactive Gas Flows," *AIAA Paper No. AIAA-88-2655*, 1988.
- ¹⁶Kustova, E. V. and Nagnibeda, E. A., "The influence of non-Boltzmann vibrational distribution on thermal conductivity and viscosity," *Molecular Physics and Hypersonic Flows*, Vol. 482, pp. 383-392, 1996.

- ¹⁷Nagnibeda, E. and Kustova, E., *Non-equilibrium Reacting Gas Flows: Kinetic Theory of Transport and Relaxation Processes*, Springer-Verlag, Berlin, Germany, 2009.
- ¹⁸Gimelshein, N. E., Gimelshein, S. F., and Levin, D. A., "Vibrational relaxation rates in the direct simulation Monte Carlo method," *Physics of Fluids*, Vol. 14, No. 12, 2002.
- ¹⁹Deschenes, T. R., Holman, T. D., Boyd, I. D., and Schwartzentruber, T. E., "Analysis of internal energy transfer within a modular particle-continuum method," *AIAA Paper No. 2009-1216*, 2009.
- ²⁰Holman, T. and Boyd, I., "Effects of Continuum Breakdown on hypersonic aerothermodynamics for reacting flow," *Physics of Fluids*, Vol. 23, 2011.
- ²¹Gupta, R., Yos, J., and Thompson, R., "A Review of Reaction Rates and Thermodynamics and Transport Properties for the 11-Species Air Model for Chemical and Thermal Nonequilibrium calculations to 30000K," *NASA TM 101528*, February 1989.
- ²²Ramshaw, J. D. and Chang, C. H., "Friction-Weighted Self-Consistent Effective Binary Diffusion Approximation," *Journal of Non-Equilibrium Thermodynamics*, Vol. 21, 1996.
- ²³Koura, K. and Matsumoto, H., "Variable soft sphere molecular model for inverse-power-law or Lennard-Jones potential," *Physics of Fluids A*, Vol. 3 pp. 2459-2465, 1991.
- ²⁴Lagarias, J., Reeds, J., Wright, M., and Wright, P., "Convergence Properties of the Nelder-Mead Simplex Method in Low Dimensions," *SIAM Journal on Optimization*, Vol. 9, No. 1, pp.112-147, 1998.
- ²⁵Nelder, J. and Mead, R., "A Simplex Method for function minimization," *Computer Journal* 7, pp. 308-313, 1965.
- ²⁶Stephani, K., Goldstein, D., and Varghese, P., "Consistent Treatment of Transport Properties for Five-Species Air DSMC/Navier-Stokes Applications," *Physics of Fluids (under review)*, 2011.
- ²⁷Chapman, S. and Cowling, T., *The Mathematical Theory of Non-Uniform Gases*, Cambridge University Press, Cambridge, 1970.
- ²⁸Holman, T. D. and Boyd, I. D., "Effects of Continuum Breakdown on hypersonic aerothermodynamics for reacting flow," *Physics of Fluids*, Vol. 23, 2011.
- ²⁹Stephani, K., Goldstein, D., and Varghese, P., "A Non-equilibrium Surface Reservoir Approach for Hybrid DSMC/Navier-Stokes Particle Generation," *Journal of Computational Physics (under review)*, 2011.
- ³⁰Wright, M. J., Candler, G. V., and Bose, D., "Data-Parallel Line Relaxation Method for the Navier-Stokes Equations," *AIAA Journal*, Vol. 36, No. 9, September 1998.
- ³¹Park, C., "On Convergence of Computation of Chemically Reacting Flows," *23rd Aerospace Sciences Meeting*, January 1985, Reno, NV 1985, pp. AIAA 85-0247.
- ³²Garcia, A., *Numerical Methods for Physics*, Prentice Hall, New Jersey, 2000.